Available online at www.eccomasproceedia.org
Eccomas Proceedia SMART (2023) 1950-1961

ECCOMAS
Proceedia

X ECCOMAS Thematic Conference on Smart Structures and Materials
SMART 2023
D.A. Saravanos, A. Benjeddou, N. Chrysochoidis and T. Theodosiou (Eds)

EFFICIENT SIMULATION OF ELECTROMECHANICAL COUPLING EFFECTS IN THIN SHELLS AT LARGE DEFORMATIONS

ASTRID PECHSTEIN*, YURY VETYUKOV† AND MICHAEL KROMMER*

*Institute of Technical Mechanics
Johannes Kepler University Linz
Altenberger Straße 69, 4040 Linz, Austria
e-mail: {astrid.pechstein|michael.krommer}@jku.at, web page: http://www.jku.at/tmech

† Institute of Mechanics and Mechatronics
TU Wien
Getreidemarkt 9, 1060 Wien, Austria
e-mail: yury.vetyukov@tuwien.ac.at

Abstract. Certain polymers are not only capable of undergoing very large deformations, but also exhibit different electromechanical coupling effects due to their dielectric or electrostrictive characteristics. The aim of the current contribution is to develop a framework for the efficient simulation of thin structures made from incompressible electroactive polymers. A thermodynamically consistent phenomenological continuum model based on the free energy density is adapted imposing the kinematic assumptions of Kirchhoff-Love shells. To make the formulation accessible to finite element simulations, the non-linear elastic shell element is extended to the present hyperelastic electromechanically coupled formulation. Computational results prove the capability of the proposed method, showing great accuracy already for coarse finite element discretizations.

Key words: shell element, electrostriction, electroactive shell, mixed finite elements

1 INTRODUCTION

Electro-active polymers show a variety of nonlinear electro-mechanical coupling effects at large deformations. These effects range from including Maxwell stresses for dielectric media, to electrostrictive effects and ferroelectric (remanent) electrical polarization strains. Different thermodynamically consistent continuum mechanics models can be derived on basis of phenomenological assumptions. We cite the monograph by Maugin [1] for a comprehensive introduction, and also the more recent review article by Dorfmann and Ogden [2] for an overview on the current state of the art in modeling electroelastica.

In actuator and sensor design, active materials are mostly used in thin layers, in order to reach sufficiently high electric fields at moderate electric potentials. From a modeling point of view,

Peer-review under responsibility of the organizing committee of SMART 2023.
doi: 10.7712/150123.9964.450600

the continuum approach is reduced to a structural formulation under assumptions concerning thickness and shear stresses. For an overview on the development of classical models in the framework of structural mechanics, we cite Vetyukov [3] or Libai and Simmonds [4]. A major challenge in the design of finite elements for these shell models is the necessity of continuously differentiable surfaces and also deformations. A different approach is the design of solid shell elements suitable for the discretization of thin structures, as e.g. proposed by Klinkel et al. [5].

In the present contribution, we develop a shell formulation for hyperelastic materials including dielectric and electrostrictive effects. Concerning the underlying continuum model, a thermodynamically consistent formulation presented in [6] is used as a vantage point. To facilitate simulations for these structures, an elastic shell element developed first by Neunteufel and Schöberl [7, 8] for elastic Koiter shells is extended to the proposed formulation. We show how to consistently represent electro-active shells within the framework of degrees of freedom available in the shell element. A great advantage of the shell element is that - apart from electrical quantities - only mid-surface displacements, membrane strains and bending moments are needed as degrees of freedom. Most importantly, mid-surface displacements need not be continuously differentiable in the finite element model, which increases the usability of the shell element greatly.

2 MODELING OF ELECTROSTRICTIVE SHELLS

We briefly discuss the basic relations in continuum modeling of nonlinear electro-elasticity, before we proceed to electro-active shells.

2.1 Electrostrictive material model

For $\Omega \subset \mathbb{R}^3$ the three-dimensional reference configuration of the body of interest, we denote $\boldsymbol{u} : \Omega \to \mathbb{R}^3$ the displacement vector, and $\mathbf{F} = \mathbf{I} + \nabla \boldsymbol{u}$ the deformation gradient. Here and in the following, all derivatives are to be understood with respect to material coordinates if not specified otherwise, moreover the ∇ operator acts row-wise on vector fields, cf. [7]. The Jacobi determinant $J = \det \mathbf{F}$ describes the transformation of volume elements. As we consider incompressible polymers throughout this work, it is assumed that $J = 1$ holds everywhere. The right Cauchy-Green tensor $\mathbf{C} = \mathbf{F}^T \cdot \mathbf{F}$ is commonly used as deformation measure in nonlinear mechanics. Work conjugate is the total Piola-Kirchhoff stress tensor $\mathbf{S}$, that relates to the total Cauchy stress in spatial configuration via $\boldsymbol{\sigma} = J^{-1}\mathbf{F} \cdot \mathbf{S} \cdot \mathbf{F}^T$.

Throughout the paper, we assume all velocities to be small as compared to the speed of light, such that the model can be developed in electrostatic regime. Concerning the electrical quantities, we denote the electric field in the spatial configuration as $\boldsymbol{e}$. It is related to the material electric field vector via the deformation gradient, $\boldsymbol{\mathcal{E}} = \mathbf{F} \cdot \boldsymbol{e}$. Given a simply connected domain Ω, Faraday's law ensures that the electric field is a gradient field, such that $\boldsymbol{\mathcal{E}} = -\nabla\varphi$ in material coordinates. In [6], we developed a material model for electrostrictive materials that used the material polarization $\boldsymbol{\mathcal{P}}$ and also an internal polarization $\boldsymbol{\mathcal{P}}_i$ as independent unknowns. These fields transform to the spatial configuration using the covariant transformation $\boldsymbol{p} = \mathbf{F} \cdot \boldsymbol{\mathcal{P}}$,

$\boldsymbol{p}_i = \mathbf{F} \cdot \boldsymbol{\mathcal{P}}_i$.

In [6], a material model for electrostrictive polymers was proposed that is based on the definition of a thermodynamic potential, $\Psi(\mathbf{C}, \boldsymbol{\mathcal{P}}, \boldsymbol{\mathcal{P}}_i, \boldsymbol{\mathcal{E}})$ that describes the augmented Helmholtz free energy density. To this end, a multiplicative splitting of the deformation gradient into an elastic and an electrostrictive part was assumed,

$$\mathbf{F} = \mathbf{F}_e \cdot \mathbf{F}_*, \tag{1}$$

with the electrostrictive part depending explicitely on the material polarization, $\mathbf{F}_* = \mathbf{F}_*(\boldsymbol{\mathcal{P}})$. Accordingly, the elastic and electrostrictive Cauchy-Green tensors are defined as $\mathbf{C}_e = \mathbf{F}_e^T \cdot \mathbf{F}_e = \mathbf{F}_*^{-T} \cdot \mathbf{C} \cdot \mathbf{F}_*^{-1}$ and $\mathbf{C}_* = \mathbf{F}_*^T \cdot \mathbf{F}_*$, respectively.

The thermodynamic potential decomposes additively into an elastic part based on the potential for incompressible Neo-Hookean solids, a polarization part modeling the dielectric properties of the material and an augmentation term containing the vacuum permittivity,

$$\Psi = \Psi_{me}(\mathbf{C}_e) + \Psi_d(\boldsymbol{p}, \boldsymbol{p}_i, \boldsymbol{e}) + \Psi_{aug}(\boldsymbol{e}), \tag{2}$$

with

$$\Psi_{me} = \frac{\mu}{2} \operatorname{tr}(\mathbf{C}_e - \mathbf{I}) = \frac{\mu}{2}(\mathbf{C} \cdot\cdot\, \mathbf{C}_*^{-1} - 3), \tag{3}$$

$$\Psi_d = -\boldsymbol{e} \cdot \boldsymbol{p} + \frac{1}{2\epsilon_0 \chi_0}(\boldsymbol{p} - \boldsymbol{p}_i) \cdot (\boldsymbol{p} - \boldsymbol{p}_i) + \Psi_p(\boldsymbol{p}_i) \tag{4}$$

$$= -\boldsymbol{\mathcal{E}} \cdot \boldsymbol{\mathcal{P}} + \frac{1}{2\epsilon_0 \chi_0}(\boldsymbol{\mathcal{P}} - \boldsymbol{\mathcal{P}}_i) \cdot \mathbf{C} \cdot (\boldsymbol{\mathcal{P}} - \boldsymbol{\mathcal{P}}_i) + \Psi_p(\mathbf{F} \cdot \boldsymbol{\mathcal{P}}_i), \tag{5}$$

$$\Psi_{aug} = -\frac{\epsilon_0}{2} \boldsymbol{e} \cdot \boldsymbol{e} = -\frac{\epsilon_0}{2} \boldsymbol{\mathcal{E}} \cdot \mathbf{C}^{-1} \cdot \boldsymbol{\mathcal{E}}. \tag{6}$$

The potential Ψ_p defines evolution and saturation of the internal polarization $\boldsymbol{p}_i$, a possible choice is provided in (30). Defining the electrostrictive part of the deformation gradient $\mathbf{F}_*$ completes the model. We propose to define $\mathbf{F}_*$ as isochoric and depending on the material polarization state, explicitely as

$$\mathbf{F}_* = \lambda_*(\mathbf{I} - \boldsymbol{e}_P \boldsymbol{e}_P) + \lambda_*^{-2} \boldsymbol{e}_P \boldsymbol{e}_P, \quad \text{with} \quad \boldsymbol{e}_P = \frac{\boldsymbol{\mathcal{P}}}{|\boldsymbol{\mathcal{P}}|} \quad \text{and} \quad \lambda_* = \left(1 + \frac{3}{2} Q \boldsymbol{P} \cdot \boldsymbol{P}\right)^{1/3}. \tag{7}$$

Constitutive relations for the work conjugate total Piola-Kirchhoff stress $\mathbf{S}$ and material dielectric displacement $\boldsymbol{\mathcal{D}}$ implied by the above potential are

$$\mathbf{S} = 2\frac{\partial \Psi}{\partial \mathbf{C}}, \qquad \boldsymbol{\mathcal{D}} = -\frac{\partial \Psi}{\partial \mathcal{E}}, \tag{8}$$

Moreover, relationships defining polarization $\boldsymbol{\mathcal{P}}$ and internal polarization $\boldsymbol{\mathcal{P}}_i$ implicitely are

$$\frac{\partial \Psi}{\partial \boldsymbol{\mathcal{P}}} = \mathbf{0}, \qquad \frac{\partial \Psi}{\partial \boldsymbol{\mathcal{P}}_i} = \mathbf{0}. \tag{9}$$

Last, we recall the principle of virtual work based on the above thermodynamic potential Ψ. Let to this end $\boldsymbol{f}$ denote external volume forces acting in Ω, while we assume that there are no surface forces and no impressed electric charges present for the sake of simplicity. For independent fields $\boldsymbol{u}$, $\boldsymbol{\mathcal{P}}$, $\boldsymbol{\mathcal{P}}_i$ and $\boldsymbol{\mathcal{E}}$, and admissible variations $\delta\boldsymbol{u}$, $\delta\boldsymbol{\mathcal{P}}$, $\delta\boldsymbol{\mathcal{P}}_i$ and $\delta\boldsymbol{\mathcal{E}}$, the principle of virtual work is obtained through variation of the total thermodynamic potential

$$\mathcal{L} = \int_\Omega (\Psi - \boldsymbol{f}\cdot\boldsymbol{u})\, dV, \tag{10}$$

$$\delta\mathcal{L} = \frac{\partial\mathcal{L}}{\partial\mathbf{C}} : \delta\mathbf{C} + \frac{\partial\mathcal{L}}{\partial\boldsymbol{\mathcal{P}}}\cdot\delta\boldsymbol{\mathcal{P}} + \frac{\partial\mathcal{L}}{\partial\boldsymbol{\mathcal{P}}_i}\cdot\delta\boldsymbol{\mathcal{P}}_i + \frac{\partial\mathcal{L}}{\partial\boldsymbol{\mathcal{E}}}\cdot\delta\boldsymbol{\mathcal{E}} \tag{11}$$

$$= \int_\Omega \left(\frac{1}{2}\mathbf{S} : \delta\mathbf{C} - \boldsymbol{f}\cdot\delta\boldsymbol{u} - \boldsymbol{\mathcal{D}}\cdot\delta\boldsymbol{\mathcal{E}}\right) dV + \int_\Omega \left(\frac{\partial\Psi}{\partial\boldsymbol{\mathcal{P}}}\cdot\delta\boldsymbol{\mathcal{P}} + \frac{\partial\Psi}{\partial\boldsymbol{\mathcal{P}}_i}\cdot\delta\boldsymbol{\mathcal{P}}_i\right) dV = 0. \tag{12}$$

2.2 Shell formulation

Subsequently, the continuum theory reviewed above shall be integrated in a nonlinear shell model. Let $\mathcal{S}$ be the shell mid-surface equipped with (unit) surface normal $\boldsymbol{N}$ at each material point. The shell of thickness t then corresponds to the three-dimensional domain $\Omega = \{\boldsymbol{X} + z\boldsymbol{N} : \boldsymbol{X} \in \mathcal{S}, z \in (-t/2, t/2)\}$. Concerning electric loading, we assume that an electric voltage is applied to electrodes that are aligned with the shell surfaces. Let $\mathbf{A}$ and $\mathbf{B}$ be the first and second metric tensor of the reference surface: the first metric tensor $\mathbf{A} = \mathbf{I} - \boldsymbol{N}\boldsymbol{N}$ realizes the projection onto the tangential plane of the reference surface, while the second metric tensor is defined as the surface gradient of the reference normal, $\mathbf{B} = -\nabla_{\mathcal{S}}\boldsymbol{N}$. Again, we use the surface gradient operator $\nabla_{\mathcal{S}}$ row-wise, as defined in [7].

Metric tensors of the deformed surface can be derived using the surface deformation gradient $\mathbf{F}_{\mathcal{S}} = \mathbf{A} + \nabla_{\mathcal{S}}\boldsymbol{u}$, where $\boldsymbol{u} : \mathcal{S} \to \mathbb{R}^3$ denotes the midsurface displacement. In Kirchhoff-Love theory, the deformed surface normal is assumed to be orthogonal to the deformed surface,

$$\boldsymbol{n} = \frac{\operatorname{Cof}\mathbf{F}_{\mathcal{S}}\cdot\boldsymbol{N}}{|\operatorname{Cof}\mathbf{F}_{\mathcal{S}}\cdot\boldsymbol{N}|}. \tag{13}$$

Using the deformed surface normal $\boldsymbol{n}$ and the derivative in the deformed surface ∇_s given through $\nabla_{\mathcal{S}} = \mathbf{F}_{\mathcal{S}}^T\cdot\nabla_s$, the first and second metric tensor of the deformed surface are defined through

$$\mathbf{a} = \mathbf{I} - \boldsymbol{n}\boldsymbol{n}, \qquad\qquad \mathbf{b} = -\nabla_s\boldsymbol{n}. \tag{14}$$

Strain measures for the surface deformation are

$$\boldsymbol{\varepsilon}(\boldsymbol{u}) = \frac{1}{2}(\mathbf{F}_{\mathcal{S}}^T\cdot\mathbf{a}\cdot\mathbf{F}_{\mathcal{S}} - \mathbf{A}), \quad \boldsymbol{\kappa}(\boldsymbol{u}) = -(\mathbf{F}_{\mathcal{S}}^T\cdot\mathbf{b}\cdot\mathbf{F}_{\mathcal{S}} - \mathbf{B}) = \mathbf{F}_{\mathcal{S}}^T\cdot\nabla_{\mathcal{S}}\boldsymbol{n} - \nabla_{\mathcal{S}}\boldsymbol{N}. \tag{15}$$

Using these strain measures, the right Cauchy-Green tensor $\mathbf{C}$ can be expressed explicitly. Under Kirchhoff-Love kinematic assumptions, its in-plane component computes as

$$\mathbf{C}_{tang} = \mathbf{A} + 2(\boldsymbol{\varepsilon} + z\boldsymbol{\kappa}). \tag{16}$$

Absence of shear deformation and incompressibility determine the out-of-plane components, such that finally

$$\mathbf{C} = \mathbf{C}_{tang} + 1/III_C^{tang}\boldsymbol{N}\boldsymbol{N}, \qquad \text{with } III_C^{tang} = |\operatorname{Cof}\mathbf{C}_{tang}\cdot\boldsymbol{N}|. \tag{17}$$

Additionally, assumptions on the distributions of electric field $\boldsymbol{\mathcal{E}}$, polarization $\boldsymbol{\mathcal{P}}$ and internal polarization $\boldsymbol{\mathcal{P}}_i$ are necessary. As we assume that electrodes are aligned orthogonal to the midsurface normal, it seems expedient to postulate these fields in direction of the midsurface normal, such that

$$\boldsymbol{\mathcal{E}} = \mathcal{E}\boldsymbol{N}, \qquad \boldsymbol{\mathcal{P}} = \mathcal{P}\boldsymbol{N}, \qquad \boldsymbol{\mathcal{P}}_i = \mathcal{P}_i\boldsymbol{N}. \tag{18}$$

In spatial setting, the appropriate transformations result in

$$\boldsymbol{e} = \mathcal{E}(III_C^{tang})^{1/2}\boldsymbol{n}, \qquad \boldsymbol{p} = \mathcal{P}(III_C^{tang})^{-1/2}\boldsymbol{n}, \qquad \boldsymbol{p}_i = \mathcal{P}_i(III_C^{tang})^{-1/2}\boldsymbol{n}. \tag{19}$$

The electric field is assumed as constant, such that $\mathcal{E} = \Delta V/t$ for a potential difference ΔV prescribed at the electrodes. Note that this voltage can also be treated as a degree of freedom, which is of interest in sensor applications.

Inserting all kinematic assumptions above (16) – (19), a quasi-3D shell energy is derived by integration through the thickness, resulting in

$$\Psi_{shell}(\boldsymbol{\varepsilon}, \boldsymbol{\kappa}, \mathcal{P}, \mathcal{P}_i, \mathcal{E}) = \int_{-t/2}^{t/2} \Psi(\mathbf{C}, \boldsymbol{\mathcal{P}}, \boldsymbol{\mathcal{P}}_i, \boldsymbol{\mathcal{E}}) dz. \tag{20}$$

In a computational setting, the integration is realized through Gaussian integration.

A Kirchhoff-Love shell problem is usually defined with $\boldsymbol{u}$ as the only independent mechanical field. Membrane strains $\boldsymbol{\varepsilon}$ and curvatures $\boldsymbol{\kappa}$ are dependent fields, defined through (15). In these definitions, not only (surface) derivatives of $\boldsymbol{u}$ are needed, e.g. in the surface deformation gradient $\mathbf{F}_S$, but also second derivatives enter through the gradient of the surface normal in the deformed configuration $\nabla_S\boldsymbol{n}$. Neunteufel and Schöberl [7] choose a different approach, which is motivated similar to the well-known Hellinger-Reissner mixed approach in continuum mechanics. In their approach, bending moments are introduced as separate unknowns. In the following, we develop a similar formulation that is inspired by the Hu-Washizu three-field theory. The correct choice of several independent unknown fields will facilitate the usage of standard nodal elements for the displacement vector instead of continuously differentiable ones.

To be precise, let the midsurface displacement $\boldsymbol{u}$, the curvature $\boldsymbol{\kappa}$ and the bending moments $\mathbf{m}$ be independent, additionally to the thickness components of the polarization vector $\mathcal{P}$, $\mathcal{P}_i$. Membrane strains are considered dependent for the moment, such that we have $\boldsymbol{\varepsilon} = \boldsymbol{\varepsilon}(\boldsymbol{u})$ as given in (15). Consequently, the Kirchhoff-Love assumption for an incompressible material yields the right Cauchy-Green tensor depending on $\boldsymbol{u}$ and $\boldsymbol{\kappa}$ according to equations (16) and

(17). Then, for a smooth surface and midsurface displacement twice weakly differentiable, $\nabla^2_{\mathcal{S}}\boldsymbol{u} \in L^2$, we define the total potential

$$\mathcal{L}(\boldsymbol{\kappa}, \boldsymbol{u}, \mathcal{P}, \mathcal{P}_i, \mathcal{E}) = \int_{\mathcal{S}} \left(\Psi_{shell} + \left(\mathbf{F}_{\mathcal{S}}^T \cdot \nabla_{\mathcal{S}}\boldsymbol{n} - \nabla_{\mathcal{S}}\boldsymbol{N} - \boldsymbol{\kappa}\right) : \mathbf{m} - \boldsymbol{f} \cdot \boldsymbol{u}\right) dS. \tag{21}$$

Variation of the potential $\mathcal{L}$ over all admissible respective fields yields the principle of virtual work for the shell problem.

3 FINITE ELEMENTS

In (21), it is necessary to have both $\boldsymbol{N}$ and $\boldsymbol{n}$ smooth, at least weakly differentiable (and thereby $\boldsymbol{u}$ twice weakly differentiable or, more classically, piecewise smooth and continuously differentiable), which is not expedient for the design of nodal shell elements. Also, structures involving kinks cannot be treated directly using the above approach.

3.1 A discrete shell formulation

In the spirit of the tangential-displacement normal-normal-stress (TDNNS) method [9, 10], Neunteufel and Schöberl [7] provided a formulation that is valid for both surfaces involving kinks as well as midsurface displacement fields that are not differentiable across element interfaces. We shortly present this idea. Let to this end $\mathcal{T} = \{T\}$ be a triangulation of $\mathcal{S}$, such that each element is smooth, and kinks are aligned with element boundaries. Let further $\mathcal{E} = \{E\}$ denote the set of all element edges. Further, we assume that the midsurface displacement $\boldsymbol{u}$ is smooth on each element and continuous across element boundaries, which is usually the case in finite element methods. Consider the part of the total potential $\mathcal{L}$ in (21) that usually requires differentiability of $\boldsymbol{N}$ and $\boldsymbol{u}$,

$$\int_{\mathcal{S}} \left(\mathbf{F}_{\mathcal{S}}^T \cdot \nabla_{\mathcal{S}}\boldsymbol{n} - \nabla_{\mathcal{S}}\boldsymbol{N}\right) : \mathbf{m}\, dS. \tag{22}$$

For piecewise smooth displacement fields, (22) can be evaluated on each element; whereever discontinuities of the normal vector $\boldsymbol{n}$ or $\boldsymbol{N}$ occur, the above formula fails, and another contribution to the work pair (22) will be necessary to model the shell correctly.

Let now T_L and T_R be two triangles connected through a common edge E. Let further $\boldsymbol{N}_R$, $\boldsymbol{N}_L$ denote the surface normals to those triangles, which are not necessarily matching on edge E. Moreover, we define $\boldsymbol{\mu}_R$ and $\boldsymbol{\mu}_L$ as the *in-plane* edge normals of edge E, compare Figure 1.

At element boundaries, bending moments are work conjugate to the change in the angle of the two adjacent surface normals. On edge E, let $\boldsymbol{\mu}_R \cdot \mathbf{m} \cdot \boldsymbol{\mu}_R = \boldsymbol{\mu}_L \cdot \mathbf{m} \cdot \boldsymbol{\mu}_L =: m_{\mu\mu}$ be the relevant component of the bending moment for a change of angle in the plane normal to E, which is in equilibrium. Its dual, the change of angle during deformation, is given through $\operatorname{acos}(\boldsymbol{n}_L \cdot \boldsymbol{n}_R) - \operatorname{acos}(\boldsymbol{N}_L \cdot \boldsymbol{N}_R)$, which motivates additional contributions of the form

$$\int_E \left(\operatorname{acos}(\boldsymbol{n}_L \cdot \boldsymbol{n}_R) - \operatorname{acos}(\boldsymbol{N}_L \cdot \boldsymbol{N}_R)\right) m_{\mu\mu}\, ds. \tag{23}$$

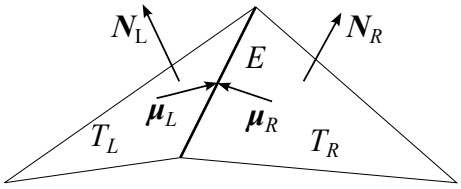

Figure 1: Definition of surface and edge normals for two adjacent elements

In [11], it was shown rigorously that, given bending moments that have a continuous in-plane normal-normal component $m_{\mu\mu}$ as above, the work pair (22) can be evaluated in distributional sense via

$$\sum_{T\in\mathcal{T}}\int_T \left(\mathbf{F}_{\mathcal{S}}^T\cdot\nabla_{\mathcal{S}}\boldsymbol{n}-\nabla_{\mathcal{S}}\boldsymbol{N}\right):\mathbf{m}\,dS+\sum_{E\in\mathcal{E}}\int_E\left(\operatorname{acos}(\boldsymbol{n}_L\cdot\boldsymbol{n}_R)-\operatorname{acos}(\boldsymbol{N}_L\cdot\boldsymbol{N}_R)\right)m_{\mu\mu}\,ds. \tag{24}$$

Evaluation through (24) is valid for midsurface displacements that are continuous across element interfaces and smooth within each element. The surface Hessian of the displacement $\mathbf{H}_{\mathcal{S}}$ allows a somewhat simpler representation of the surface integrals, see [7] for a proof,

$$\int_T \left(\mathbf{F}_{\mathcal{S}}^T\cdot\nabla_{\mathcal{S}}\boldsymbol{n}-\nabla_{\mathcal{S}}\boldsymbol{N}\right):\mathbf{m}\,dS=-\int_T\left(\mathbf{H}_{\mathcal{S}}+(1-\boldsymbol{N}\cdot\boldsymbol{n})\nabla_{\mathcal{S}}\boldsymbol{N}\right):\mathbf{m}\,dS \tag{25}$$

$$\text{with } \mathbf{H}_{\mathcal{S}}=\sum_{i=1}^{3}n_i(\nabla_{\mathcal{S}}u_i). \tag{26}$$

As a result, the total potential $\mathcal{L}$ from (21) is replaced by a formulation that is valid for continuous midsurface displacements and bending moments with continuous in-plane normal-normal component $m_{\mu\mu}=\boldsymbol{\mu}_R\cdot\mathbf{m}\cdot\boldsymbol{\mu}_R=\boldsymbol{\mu}_L\cdot\mathbf{m}\cdot\boldsymbol{\mu}_L$,

$$\mathcal{L}(\boldsymbol{\kappa},\boldsymbol{u},\mathbf{m},\boldsymbol{\mathcal{P}},\boldsymbol{\mathcal{P}}_i,\boldsymbol{\mathcal{E}})=\int_{\mathcal{S}}\left(\Psi_{shell}-\boldsymbol{f}\cdot\boldsymbol{u}\right)dS \tag{27}$$

$$-\sum_{T\in\mathcal{T}}\int_T\left(\boldsymbol{\kappa}+\mathbf{H}_{\mathcal{S}}+(1-\boldsymbol{N}\cdot\boldsymbol{n})\nabla_{\mathcal{S}}\boldsymbol{N}\right):\mathbf{m}\,dS \tag{28}$$

$$+\sum_{E\in\mathcal{E}}\left(\operatorname{acos}(\boldsymbol{n}_L\cdot\boldsymbol{n}_R)-\operatorname{acos}(\boldsymbol{N}_L\cdot\boldsymbol{N}_R)\right)m_{\mu\mu}\,ds. \tag{29}$$

3.2 Finite element discretization

We shortly comment on the technical aspects of a finite element implementation, such as the choice of approximation spaces, shape functions or degrees of freedom.

Standard nodal displacement elements can be used for a finite element formulation based on (27). Thus, $\boldsymbol{u}$ can be discretized using standard nodal elements of order k on each triangular element T. Also quadrilaterals can be treated, but here the definition of shape functions becomes

Table 1: Material parameters for polyurethane, taken from [6]

$\mu/\mathrm{N\,m^{-2}}$	$\chi_0/1$	$\chi_i/1$	$Q/\mathrm{C^2\,m^4}$	$p_{sat}/\mathrm{C\,m^{-2}}$	$n_{sat}/1$
19.83×10^6	1.566	7.134	150.25×10^3	295×10^{-6}	10

more involved (compare [12] or [13] for the three-dimensional case), so we do not address this case in the current contribution.

Bending moments $\mathbf{m}$ must be chosen such that they form a stable pair when combined with midsurface displacements, in the sense that an inf-sup condition is satisfied (see [14] for a comprehensive analysis on finite element methods for mixed problems). Moreover, the equilibrium constraint $m_{\mu\mu} = \boldsymbol{\mu}_R \cdot \mathbf{m} \cdot \boldsymbol{\mu}_R = \boldsymbol{\mu}_L \cdot \mathbf{m} \cdot \boldsymbol{\mu}_L$ must be met on shape function level. Finite element basis functions satisfying this constraint on surfaces have been constructed in [11]. As an alternative, it is proposed to use piecewise discontinuous bending moments and add the edge equilibrium constraint via additional Lagrangian multipliers on surface edges. [7] refer to this workaround as hybridization. In this case, bending moments are discretized using any polynomial basis of order $k-1$ for the tensor components on each triangle T, and also the Lagrangian multipliers are polynomial of order $k-1$ on each edge E in the mesh.

Concerning curvatures, there are no restrictions on the regularity of the finite element function; we propose to use piecewise polynomial tensor components of order $k-1$, as for the bending moments.

Last, polarization and internal polarization can be approximated element-wise polynomial. In the computational results presented below, again piecewise polynomial approximations of order $k-1$ have been used.

In [8], Neunteufel and Schöberl have shown that the shell element as described above suffers from membrane locking, unless a projection of the membrane strains $\boldsymbol{\varepsilon}$ to the Regge space is done. Based on the metric introduced by Regge [15] for the Einstein field equations, finite elements have been developed since, see [16, 17] for the lowest order case and [18] for arbitrary order elements. We do not go into details concerning the projection. However, it is important to note that it is a purely local operation that is done on each element and edge in the mesh independently.

4 EXAMPLES

Computational results for two different problems are presented. In both cases, we use polyurethane as a material, and take material parameters as identified in [6]. These parameters are collected in Table 1. The thermodynamic potential $\Psi_p(\boldsymbol{p}_i)$, that defines the evolution and saturation of the internal polarization $\boldsymbol{p}_i = (III_C^{tang})^{-1/2}\mathcal{P}_i\,\boldsymbol{n}$, is defined implicitely through its rate,

$$\Psi_p(\boldsymbol{p}_i) = \tilde{\Psi}_p(|\boldsymbol{p}_i|), \qquad \text{with } \tilde{\Psi}_p'(p) = \frac{1}{\epsilon_0\chi_i}\frac{p}{\left(1-(p/p_{sat})^{n_{sat}}\right)^{1/n_{sat}}}. \tag{30}$$

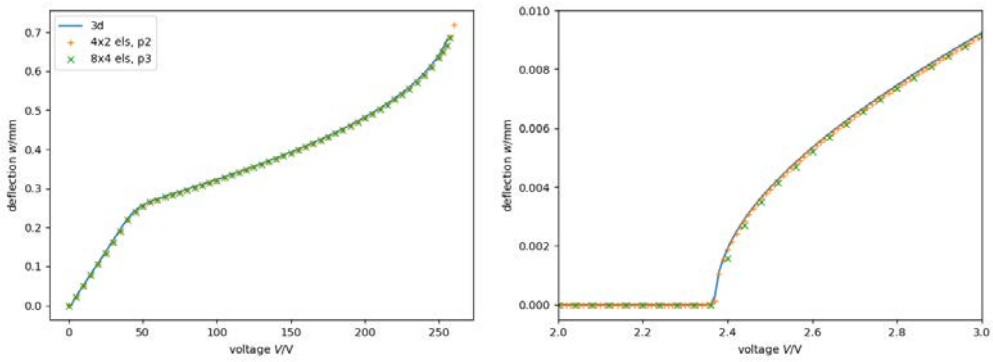

Figure 2: Buckling of electrostrictive plate: midpoint deflection over applied voltage up to breakdown voltage (left) and in buckling region (right), using two different finite element meshes and approximation orders. Comparison to results from [6] indicated "3d".

4.1 Buckling of electrostrictive plate

To show the capability of the shell element, in our first example we present results based on a setup described in [6]. A plate made from a single layer of polyurethane, of dimensions $L \times W \times H = 4\,\mathrm{mm} \times 2\,\mathrm{mm} \times 0.01\,\mathrm{mm}$ is clamped on both ends, compare Figure 2.

We use two different equidistant structured triangular meshes, one using four by two elements, the other one using eight by four elements for one quarter of the electroactive shell. We compare the behavior when using second order elements on the coarse mesh and third order elements on the fine mesh. For the coarse discretization, we end up with 867 degrees of freedom for all discretized fields (including midsurface displacement, curvature, membrane strain, polarization and internal polarization), whereas for the fine discretization we count 6657 degrees of freedom in total.

The electric field is raised from zero up to breakdown voltage. In the original publication, buckling was observed to initiate at $2.37\,\mathrm{V}$. In the current setup, we observe a deviation from the plane configuration at the same voltage for both the coarse and the fine mesh. Concerning breakdown, the electric field can be raised up to $255\,\mathrm{V}$ for the fine and $260\,\mathrm{V}$ for the coarse mesh, which is in good agreement with $255.5\,\mathrm{V}$ observed in the original contribution.

4.2 Actuated cylinder

As a second example, we consider a cantilevered cylindrical tube of length $L = 100\,\mathrm{mm}$, radius $r = 10\,\mathrm{mm}$ and wall thickness $t = 0.5\,\mathrm{mm}$. The cylinder is actuated by applying a voltage to electrodes that cover internal and external surface at a distance ranging from $l_1 = 5\,\mathrm{mm}$ to $l_2 = 50\,\mathrm{mm}$, thereby generating an integrated pump. A distributed vertical tip load of $1000\,\mathrm{N\,m^{-2}}$ acts on the free end, which results in a total load of $0.01\pi\mathrm{N}$. Moreover, an assumed vertical volume load of $9810\,\mathrm{N\,m^{-3}}$ mimicks gravity.

Two finite element models were generated, one using two layers of prismatic elements, and another one using the proposed shell elements. The prismatic mesh consists of 6378 elements

that are refined towards the interface between actuated and non-actuated parts, whereas we use two different shell meshes: a fine mesh that is generated using the same mesh size parameters as the prismatic mesh, consisting of 3342 triangular elements, and a very coarse mesh consisting of 134 triangles. The volume model is considered for reasons of verification, third order Taylor-Hood displacement-pressure elements were used, and also third order elements for the electric potential. This resulted in a total of 324985 inter-element coupling degrees of freedom. Using second order shell elements (i.e. $k = 2$) on the fine mesh, 50130 coupling degrees of freedom were needed, whereas the coarse mesh discretized with third-order shell elements (i.e. $k = 3$) leads to a system with 3618 unknowns.

Considering the mechanical loads only, the cylinder bends, with a mean vertical displacement of the tip surface of $-0.16671\,\mathrm{mm}$ as computed using the accurate volume model. For the shell models, values of $-0.16720\,\mathrm{mm}$ and $-0.16788\,\mathrm{mm}$ are computed on the fine and coarse mesh, respectively. As a voltage is applied to the electrodes, we see an asymmetric build-up of polarization, as the pre-stress/pre-deformation due to bending leads to a stronger increase in polarization in the top half of the cylinder, where the material is elongated. In the bottom half, where we have compression due to the external load, evolution of polarization is inhibited. We compare the resulting polarization state for the three different models visually in Figure 3. Figure 4 additionally displays the computed mean deflection in vertical direction, as well as the relative error. At $V = 1500\,\mathrm{V}$, for the reference model a deflection of $-0.82469\,\mathrm{mm}$ is computed, while the shell formulations yield $-0.81940\,\mathrm{mm}$ on the fine and $-0.81289\,\mathrm{mm}$ on the coarse mesh, respectively. Throughout the simulation, the relative error in deflection is below 1% for the fine and below 1.5% for the coarse mesh.

REFERENCES

[1] G. Maugin, *Continuum Mechanics of Electromagnetic Solids*. North-Holland, 1988.

[2] L. Dorfmann and R. W. Ogden, "Nonlinear electroelasticity: material properties, continuum theory and applications," *Proceedings of the Royal Society A: Mathematical, Physical and Engineering Sciences*, vol. 473, no. 2204, p. 20170311, 2017.

[3] Y. Vetyukov, *Nonlinear mechanics of thin-walled structures: asymptotics, direct approach and numerical analysis*. Springer Science & Business Media, 2014.

[4] A. Libai and J. Simmonds, *The Nonlinear Elasticity of Elastic Shells*. Cambridge, United Kingdom: Cambridge University Press, 2005.

[5] S. Klinkel, S. Zwecker, and R. Müller, "A solid shell finite element formulation for dielectric elastomers," *Journal of Applied Mechanics*, vol. 80, no. 2, 2013.

[6] A. Pechstein, M. Krommer, and A. Humer, "Modeling and numerical simulation of electrostrictive materials and structures," *Smart Structures and Systems*, vol. 30, no. 3, pp. 221–237, 2022.

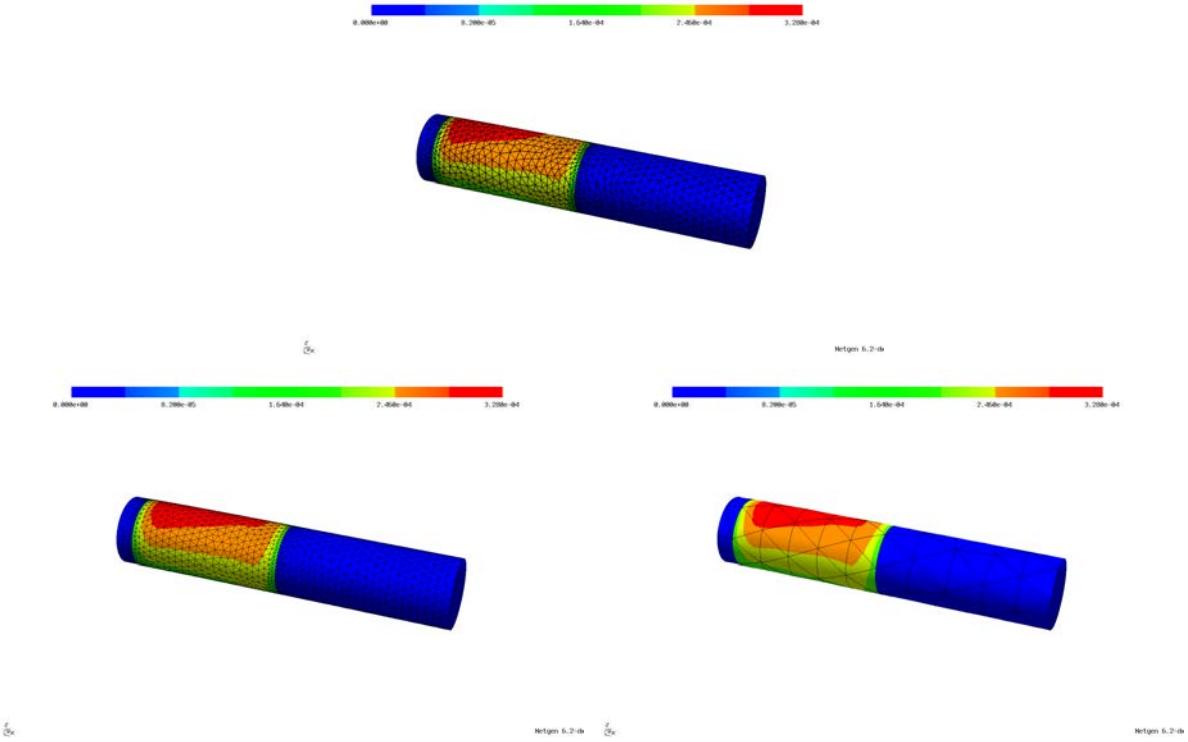

Figure 3: Actuated cylinder: Absolute value of material polarization $|\mathcal{P}|$ at an applied voltage of $1500\,\mathrm{V}$. Reference solution on prismatic mesh (top), shell elements with $k = 2$, 50130 coupling degrees of freedom (bottom left), and with $k = 3$, 3618 coupling degrees of freedom (bottom right).

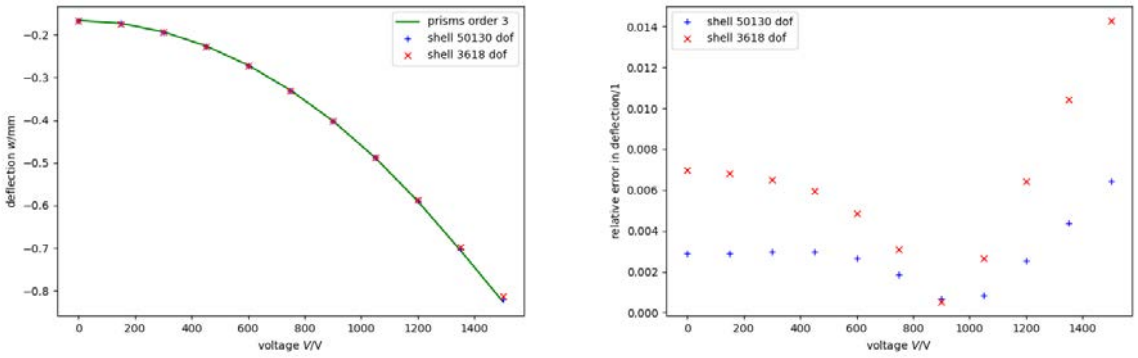

Figure 4: Actuated cylinder: Deflection w over applied voltage V (left) and relative error in deflection (right), comparing shell models to 3d discretization.

[7] M. Neunteufel and J. Schöberl, "The hellan–herrmann–johnson method for nonlinear shells," *Computers & Structures*, vol. 225, p. 106109, 2019.

[8] ——, "Avoiding membrane locking with regge interpolation," *Computer Methods in Applied Mechanics and Engineering*, vol. 373, p. 113524, 2021.

[9] A. Pechstein and J. Schöberl, "Tangential-displacement and normal-normal-stress continuous mixed finite elements for elasticity," *Mathematical Models and Methods in Applied Sciences*, vol. 21, no. 8, pp. 1761–1782, 2011.

[10] ——, "The TDNNS method for Reissner–Mindlin plates," *Numerische Mathematik*, vol. 137, no. 3, pp. 713–740, 2017.

[11] M. Neunteufel, "Mixed finite element methods for nonlinear continuum mechanics and shells," Ph.D. dissertation, TU Vienna, Austria, 2021.

[12] A. Pechstein and J. Schöberl, "Anisotropic mixed finite elements for elasticity," *International journal for numerical methods in engineering*, vol. 90, no. 2, pp. 196–217, 2012.

[13] M. Neunteufel, A. S. Pechstein, and J. Schöberl, "Three-field mixed finite element methods for nonlinear elasticity," *Computer Methods in Applied Mechanics and Engineering*, vol. 382, p. 113857, 2021.

[14] D. Boffi, F. Brezzi, M. Fortin *et al.*, *Mixed finite element methods and applications*. Springer, 2013, vol. 44.

[15] T. Regge, "General relativity without coordinates," *Nuovo Cim*, vol. 19, pp. 558–571, 1961.

[16] S. H. Christiansen, "A characterization of second-order differential operators on finite element spaces," *Mathematical Models and Methods in Applied Sciences*, vol. 14, no. 12, pp. 1881–1892, 2004.

[17] ——, "On the linearization of regge calculus," *Numerische Mathematik*, vol. 119, pp. 613–640, 2011.

[18] L. Li, "Regge finite elements with applications in solid mechanics and relativity," Ph.D. dissertation, University of Minnesota, 2018.